ADVANCED OPTICAL MATERIALS
www.advopticalmat.de

Unlocking Spin Dynamics: Spin-Orbit Coupling Driven Spin State Interconversion in Carbazole-Containing TADF Emitters

Annika Morgenstern, Jonas Weiser, Lucas Schreier, Konstantin Gabel, Tom Gabler, Alexander Ehm, Daniel Beer, Nadine Schwierz, Ulrich T. Schwarz, Kirsten Zeitler, Carsten Deibel, Dietrich R. T. Zahn, Christian Wiebeler, and Georgeta Salvan**

The determination of transport mechanisms in organic light-emitting diodes (OLEDs) is crucial for optimizing device performance. Magnetic field measurements enable the differentiation of spin state interconversion mechanisms, but data interpretation remains challenging. Here, experimental and theoretical investigations are combined to provide a comprehensive understanding of the underlying processes. This study systematically compares three cyanoarene-based emitters with different singlet–triplet gaps (ΔE_{ST}) to explore factors influencing reverse intersystem crossing (RISC). The comparison of all-^{1}H and all-^{2}H 4CzIPN isotopologues confirms that RISC is governed by spin-orbit coupling (SOC) rather than hyperfine interactions. Magnetic field-dependent measurements reveal that charge transport in OLED devices is driven by triplet-charge annihilation in 3CzClIPN and 4CzIPN, while triplet–triplet annihilation dominates for 5CzBN. Theoretical calculations further indicate that SOC-mediated RISC in 3CzClIPN and 4CzIPN can additionally occur via a T_2 intermediate state with an activation energy distinct from ΔE_{ST}. A temperature-dependent analysis of the devices was conducted to quantify this activation energy and compare it with the computational findings. These findings establish key correlations between activation energy, spin dynamics, and magnetic field effects in TADF emitters, advancing the understanding of excitonic processes in OLEDs.

1. Introduction

Organic light-emitting diodes (OLEDs) play a crucial role in optoelectronic applications, including flat-panel displays, white light sources,[1,2] and wearable electronics.[3–6] Beyond these applications, OLEDs are also attracting growing interest in sensor technology[7] and biomedicine.[3,6]

In recent years, organic thermally activated delayed fluorescence (TADF) materials have gained significant attention due to their intrinsic ability to enable reverse intersystem crossing (RISC) from the triplet to the singlet excited states.[2,8,9] This process allows for a theoretical internal quantum efficiency of up to 100% without the need for heavy atoms.[10] By tuning donor and acceptor units, the energy gap between the singlet and triplet states (ΔE_{ST}) can be adjusted. To efficiently harness triplet excitons, a small ΔE_{ST} in the range of thermal energy at room temperature is required.[11,12] If ΔE_{ST} is too large, RISC becomes inefficient, reducing overall device performance.[13–15] However,

A. Morgenstern, L. Schreier, K. Gabel, A. Ehm, D. R. T. Zahn, G. Salvan
Semiconductor Physics, Institute of Physics
Chemnitz University of Technology
09126 Chemnitz, Germany
E-mail: georgeta.salvan@physik.tu-chemnitz.de

J. Weiser, N. Schwierz, C. Wiebeler
Computational Biology, Institute of Physics
University of Augsburg
86159 Augsburg, Germany
E-mail: christian.wiebeler@uni-a.de

T. Gabler, K. Zeitler
Organic Chemistry and Catalysis, Institute of Organic Chemistry
Leipzig University
04103 Leipzig, Germany

K. Gabel, U. T. Schwarz
Experimental Sensor Science, Institute of Physics
Chemnitz University of Technology
09126 Chemnitz, Germany

D. Beer, C. Deibel
Optics and Photonics of Condensed Matter, Institute of Physics
Chemnitz University of Technology
09126 Chemnitz, Germany

D. R. T. Zahn, G. Salvan
Materials, Architecture and Integration of Nanomembranes (MAIN)
Chemnitz University of Technology
09126 Chemnitz, Germany

The ORCID identification number(s) for the author(s) of this article can be found under https://doi.org/10.1002/adom.202501504

DOI: 10.1002/adom.202501504

the exact mechanism behind the spin state interconversion process remains a topic of debate and strongly depends on the choice of material.[16,17] For exciplex-based TADF materials, where charge-transfer complexes are formed between two distinct molecules, the dominant spin state interconversion mechanism is often attributed to the Δ*g*-mechanism or hyperfine induced spin-mixing.[18,19] In contrast, these effects appear to be less significant in excitonic TADF systems. Recently, Wang et al.[16] proposed that spin-orbit coupling (SOC) plays a major role in facilitating the spin state interconversion process and Gibson et al.[20] highlighted the critical role of vibronic coupling in enabling efficient RISC in TADF materials.[21] However, determining the underlying spin state interconversion mechanism experimentally is challenging. To investigate these interactions, magnetic fields are often used to induce Zeeman splitting, thereby lifting the degeneracy of the triplet states. Depending on the dominant spin state interconversion mechanism, the broadening of the magnetic field effect curves changes accordingly. These magnetic field effects (MFEs) are generally quantified using the following equation:

$$\mathrm{MFE} = \frac{MFE(B) - MFE(B=0)}{MFE(B=0)} \tag{1}$$

MFEs have been exploited to gain insight into the spin dynamics of emitter materials.[16,22,23] The MFE response is most commonly attributed to hyperfine interactions (HFIs),[23,24] the Δ*g*-mechanism,[19] and second-order processes,[25,26] such as triplet–triplet annihilation (TTA) or triplet-charge annihilation (TCA).[17] In the case of TADF materials, MFEs have also been suggested to affect the RISC process.[16,18,19] Each mechanism exhibits a distinct fingerprint MFE curve, aiding in identifying the dominant effect influencing charge transport.[16]

If the device is electrically biased, the electrons and holes injected from the electrodes can recombine and form weakly bound polaron pairs (PP) as either singlets (PP_1) or triplets (PP_3) on neighboring molecules.[16,27,28] PP_3 includes the degenerate states $PP_{3,+}$, $PP_{3,0}$, and $PP_{3,-}$. If the exchange interaction energy between electrons and holes is weak, spin state interconversion is facilitated by HFI, namely intersystem crossing (ISC) ($PP_1 \rightarrow PP_3$) and RISC ($PP_3 \rightarrow PP_1$).[16,29]

Generally, the coupling strength, originating from either HFI or SOC, can be directly linked to a characteristic magnetic field via the Zeeman energy:

$$B_0 = \frac{E_{\mathrm{coup}}}{g_{\mathrm{e-h}}\mu_B} \tag{2}$$

where the energy E_{coup} is determined using the Planck relation, which can be considered as the energy of the coupling strength:

$$E = hc\tilde{\nu} \tag{3}$$

with h being the Planck constant, c the speed of light, and $\tilde{\nu}$ the wavenumber. Here, $g_{\mathrm{e\text{-}h}}$ represents the Landé factor of an electron-hole pair, and μ_B denotes the Bohr magneton. E_{coup} is proportional to B_0, so the broadening of the MFE curve can be directly associated with an increased coupling strength, as the characteristic magnetic field B_0 is increased (Equation 7, vide infra). HFI in organic molecules is generally weak, causing a characteristic magnetic field (⩽10 mT), while a broader response is expected if SOC dominates.[16,30]

In addition to the spin state interconversion analysis, the application of an external magnetic field allows for the differentiation between various charge carrier transport mechanisms, as they exhibit distinct fingerprint responses.[16,31] In TCA, a T_1 exciton collides with a charge carrier (q), which makes the carrier scatter and the T_1 states quench ($T_1 + q \rightarrow q' + S_0$).[16,32] As Wang et al.[16] explained, the Zeeman splitting of the T_1 state causes a decrease of the rate constant of the TCA process when applying an external magnetic field. This means that the external magnetic field can lower the probability for TCA, therefore enhancing the T_1 population. Consequently, more charge carriers can contribute to the RISC process, enhancing the magnetoelectroluminescence (MEL) response.[16,31] It is important to note that the spin state interconversion can occur only from the $T_{n,0}$ state to the excited singlet state, since intra-triplet state mixing is suppressed according to the lifting of the degeneration of triplet states due to the applied magnetic field.

The TTA process can be described as $T_1 + T_1 \rightarrow S_n + S_0$ and is also affected by the Zeeman splitting of the T_1 state. Below $|B| <$ 20 mT,[16,17,31,33] the zero-field splitting is stronger than the Zeeman splitting. Consequently, the annihilation rate constant of the T_1 state is increased, which is reflected in an increase in the MEL response. Conversely, by increasing the magnitude of the magnetic field to $|B| > 20$ mT, the Zeeman splitting becomes stronger than the zero-field splitting. Consequently, the annihilation rate constant decreases, and the MEL response is decreased.[16]

Differentiating between these mechanisms in emitter materials using MFEs can be challenging, often leading to overfitting in an attempt to account for all observed effects (e.g. TCA, TTA, RISC, ISC).[16,31,32] In the case of the carbazole-based molecules under study, we propose a simple model based on the combination of only two Lorentzian fitting functions, which replicates our measured data and is in line with our theoretical investigations. To reduce the impact of all materials other than the emissive carbazole-based molecules, we fabricated simple layer stack devices containing only three organic layers, namely the hole-transport layer (PEDOT:PSS), the emissive layer (carbazole-based cyanoarene molecules), and the electron-transport layer (TPBi). Furthermore, our advanced measurement setup, coupled with its original software, enabled a rigorous statistical analysis, enhancing the reproducibility and reliability of our results. A comprehensive description of the hard- and software components of the MFE measurement setup, along with the analysis process, is provided in the Supporting Information (see Section S1.1., Experimental Apparatus and Analysis).

While differentiating between the mechanisms present in emitter materials can be easier from a computational point of view, computational approaches struggle with different problems when it comes to the description of spin state interconversion processes. (Spin) dynamics in excited states are challenging to model due to the complex net of state interactions[34] and long timescales needed to simulate the RISC process. In this work, we present a workflow that allows for the discussion of spin dynamics between the potential energy surfaces (PESs) of the involved excited states without the need for explicit excited state molecular dynamics simulations. A key component of this

analysis is the identification of points of contact between different PESs, namely minimum energy crossing points (MECPs) between states of different spin multiplicity and minimum energy conical intersections (MECIs) between states of the same multiplicity.[35,36] When two PESs corresponding to different electronic states intersect, the emerging energy degeneracy allows for efficient transitions between these states. Consequently, knowing the location of these intersections enables the evaluation of dynamic processes without requiring molecular dynamics simulations.

The intersection of two PESs is defined by the vectors along which the energy degeneracy is lifted, the gradient difference vector (*GDV*) and the derivative coupling vector (*DCV*):[35,37]

$$GDV = \frac{\partial(E_1 - E_2)}{\partial q} \tag{4}$$

$$DCV = \langle \Psi_1 | \left(\frac{\partial}{\partial q} \right) | \Psi_2 \rangle = \frac{\langle \Psi_1 | \left(\frac{\partial \hat{H}}{\partial q} \right) | \Psi_2 \rangle}{E_1 - E_2} \tag{5}$$

with the latter determining how strongly the electronic wavefunctions change with respect to a change in the nuclear coordinates q. 2D subspace spanned by the *GDV* and the *DCV* is also called the branching plane.

For MECPs, transitions occur between states of different spin multiplicities, meaning the *DCV* is zero as there is no direct derivative coupling between the wavefunctions. Instead, transitions proceed via SOC. In this case, the characteristic double cone shape of the intersection is unfolded and the degeneracy is extended from a single point to a 1D hyperline. To find the energy minimum on this hyperline, i.e., the MECP, Bearpark et al. proposed the gradient projection method.[35] Here, the GDV is constrained to stay on the hyperline while the gradient of E_2 is projected onto the remaining orthogonal space and minimized.

In the case of MECI optimization, both the *GDV* and the *DCV* are necessary. However, as the calculation of the *DCV* is not widely available for all quantum chemistry methods and can be costly or potentially unreliable depending on the accuracy of the method, Maeda et al. developed an approach that does not rely on the explicit *DCV*.[36] The 2D branching plane is instead updated in a gradient projection framework using only the *GDV*. At each optimization step, the branching plane is represented by two orthonormal unit vectors: A unit vector x parallel to the *GDV* and a unit vector y perpendicular to it that needs to be estimated through the updating method as a surrogate for the *DCV*. The method relies on the fact that even with an inaccurate initial y, as the optimization proceeds around the region of the conical intersection, x (and thus the *GDV*) minimizes the energy difference between the electronic states and leads towards the energy minimum. This induces changes that allow the iterative algorithm to refine the estimation of y.

By combining the outlined computational and experimental approaches, we can provide a comprehensive picture of the interconversion processes in carbazole-containing TADF emitters.

2. Results and Discussion

2.1. Device Fabrication

The specific layer structure for all fabricated devices can be found in **Figure 1**a,b. Throughout this study, the three cyanoarene molecules 2,4,6-Tri(9*H*-carbazol-9-yl)-5-chloroisophthalonitrile (**3CzClIPN**), 1,2,3,5-Tetrakis(carbazol-9-yl)-4,6-dicyanobenzene (**4CzIPN**), and Penta-carbazolylbenzonitrile (**5CzBN**) were compared as bare molecular devices as well as embedded in a host-guest system with 4,4′ -Bis(*N*-carbazolyl)-1,1′ -biphenyl (CBP) as host material (host:guest ratio 9:1). Their molecular structure is depicted in Figure 1c–f with the respective calculated adiabatic ΔE_{ST} for the TADF emitters (*cf.* (c–e)). An overview of the employed quantum chemical methods is given in the Experimental Section at the end of this article. Additional details are provided in the Supporting Information. ΔE_{ST} can be reduced by strengthening the acceptor unit(s).[38] In contrast, the introduction of carbazole (donor) units increases ΔE_{ST}. This is closely tied to the influence of donor and acceptor units on the frontier orbitals (**Figure 2**). Since RISC in TADF molecules depends on efficient energy transfer, a small ΔE_{ST} is preferred for optoelectronic applications such as OLEDs.[2]

To assess the quality of the band alignment (*cf.* Figure S13, Supporting Information), the positions of the highest occupied molecular orbital (HOMO) and lowest unoccupied molecular orbital (LUMO) were calculated with density functional theory (DFT) for all molecules at the B3LYP-D3/def2-SVPD level of theory. These results were then compared to values obtained through a combination of low-energy inverse photoemission (LEIPES) and ultraviolet photoemission spectroscopy (UPS) for validation. The computational results are shown in Figure 2a, illustrating a continuous increase in the HOMO–LUMO gap from 3CzClIPN to 5CzBN. Additionally, both the HOMO and LUMO positions exhibit an upward shift in energy, following this same trend. Figure 2b shows the experimentally determined values of the HOMO and LUMO onsets and the work function W for 4CzIPN with respect to the vacuum energy E_{vac} from UPS and LEIPES measurements. The work function determined for the Au substrate is (4.57 ± 0.05) eV, which is significantly lower than typical values from literature (e.g., 5.4 eV).[39] This is due to the presence of an adventitious carbon layer, which was not removed before the deposition of 4CzIPN to keep conditions similar to the samples that were prepared outside ultra high vacuum (UHV) conditions using spin-coating. With increasing organic film thickness, a progressive shift of the work function W corresponding to a movement of the Fermi level towards the vacuum level can be observed. This is accompanied by an apparent opening of the HOMO–LUMO gap, which saturates near a film thickness of 8 nm. Such effects were often observed in relation to ultra-thin films of organic semiconductors on metallic substrates. In phthalocyanine molecules, this was associated with the formation of an image charge potential, due to the mirroring of the molecular electron cloud in the conductive substrate.[40] The energy parameters determined for the largest film thickness can be considered as the values of the bulk material. They amount to EA = (2.88 ± 0.03) eV for the electron affinity, IE = (6.0 ± 0.1) eV for the ionization energy, and W = (3.74 ± 0.05) eV. This adds up to a transport bandgap of (3.12 ± 0.13) eV. The

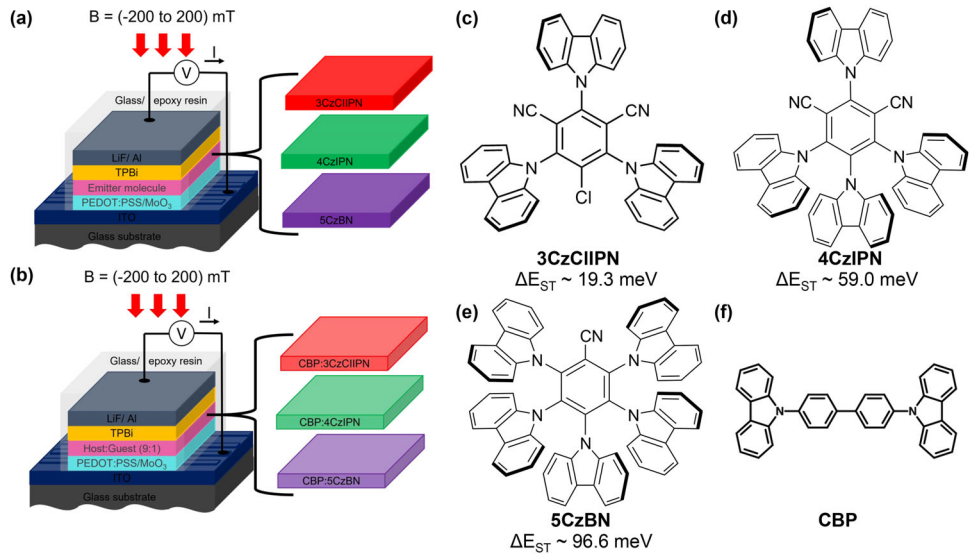

Figure 1. Layer stacks of the devices fabricated using a) the bare emitters, and b) a host–guest system, along with the molecular structures of the TADF emitters in (c)–(e). The corresponding ΔE_{ST}, obtained from time-dependent density functional theory calculations (see Computational Details in the Supporting Information), are also provided for c) 3CzClIPN, d) 4CzIPN, and e) 5CzBN. The molecular structure of the host compound CBP is depicted in (f).

uncertainty of *EA* is given here by the standard deviation of the values determined from measurements under different conditions, i.e., using different bandpass filters (BPFs), as proposed by Sugie et al.[41] The measured Fermi level being closer to the LUMO onset than to the HOMO onset suggests an n-type character of the organic film. The obtained values for the electron affinity and ionization energy can be associated with the LUMO and HOMO position, respectively. The obtained values are in very good agreement with the DFT results. The bulk energy parameters for 3CzClIPN and 5CzBN were determined for 11 nm and 16.5 nm thick films, respectively. They amount to *EA*(3CzClIPN) = (3.23 ± 0.14) eV, *EA*(5CzBN) = (3.00 ± 0.16) eV, *IE*(3CzClIPN) = (6.33 ± 0.10) eV, *IE*(5CzBN) = (5.94 ± 0.10) eV, *W*(3CzClIPN) = (4.01 ± 0.05) eV, and *W*(5CzBN) = (3.96 ± 0.05) eV. A more detailed description of the UPS, XPS, and LEIPES experiments and their analysis can be found in the Supporting Information (*cf.* Section S1.1.4 and Figures S8– S12, Supporting Information).

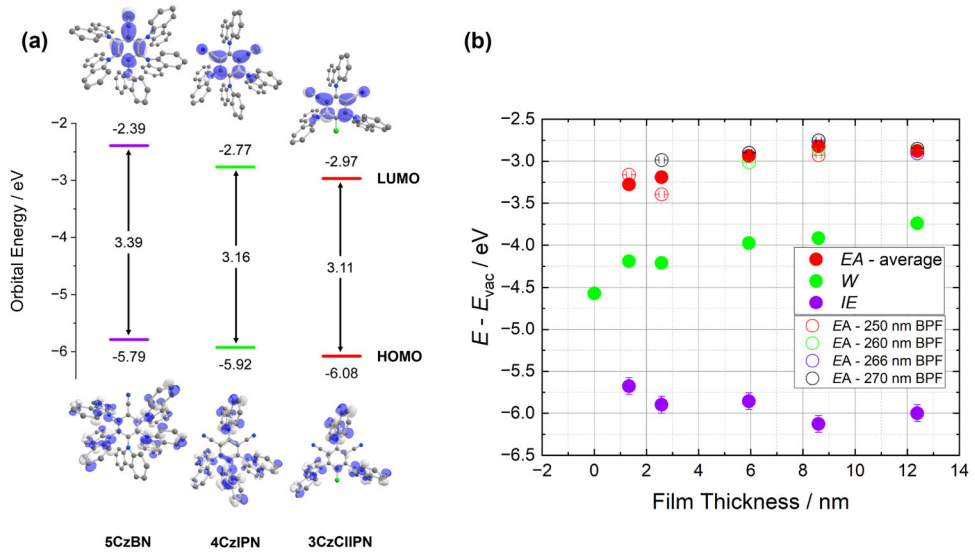

Figure 2. a) HOMOs and LUMOs of 5CzBN, 4CzIPN, and 3CzClIPN with corresponding absolute orbital energies and corresponding HOMO–LUMO gaps obtained from density functional theory calculations at the B3LYP-D3/def2-SVPD level of theory. b) Thickness-dependent energy diagram of the experimentally determined HOMO and LUMO onsets of 4CzIPN on Au, expressed by the ionization energy *IE* and the electron affinity *EA*, as well as its work function *W*, with respect to the vacuum energy E_{vac}. Multiple values of *EA* measured with different bandpass filters (BPFs) are shown to evaluate the statistical significance of the determined parameters.

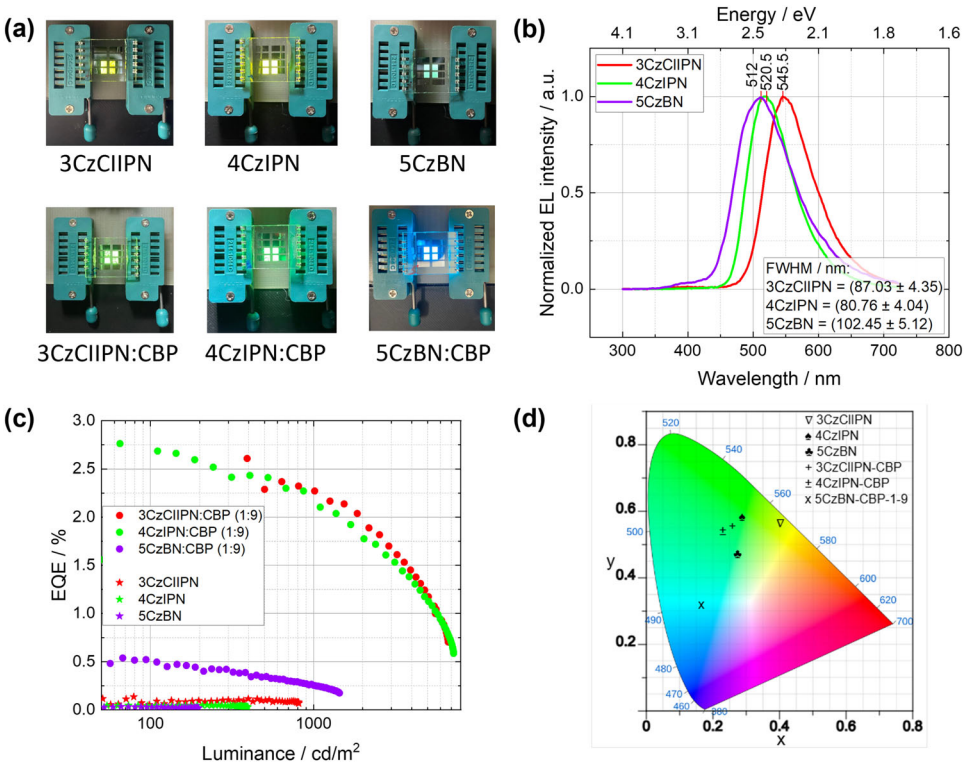

Figure 3. a) Images of the devices fabricated in this work with four of the 8 pixels emitting light, (b) shows the EL response for the bare molecules depicted in (a). c) EQE for the simple layer stack with the bare molecules compared to the host-guest system, containing CBP as a host material and showing a strong enhancement. d) CIE chromaticity diagram extracted from the EL response (*cf.* Figure 3b).

2.2. Optoelectronic Characterization

The difference in emitted color is visible to the naked eye when comparing the light emission of the investigated bare molecular devices (*cf.* **Figure** 3a). As can be seen in Figure 3b, the electroluminescence (EL) response shows a blue shift as the number of carbazole units increases. This can be explained by an increase in the HOMO–LUMO gap from 3CzClIPN to 5CzBN as shown in Figure 2. Since the HOMO is localized on the carbazole donor units and the LUMO on the acceptor unit, changes in the donor or acceptor composition directly affect the energy gap. The trend from 3CzClIPN to 5CzBN shows that successively adding carbazole donor units leads to a steady increase in the energy of the HOMO due to the increasing electron-donating effect of the electron-rich carbazole moiety. Conversely, starting from 5CzBN and going to 3CzClIPN, introducing electron-withdrawing groups such as CN and Cl to the acceptor unit lowers the energy of the LUMO. Notably, while the relative energy increase of the HOMOs remains constant across the series from 3CzClIPN to 5CzBN, the relative energy decrease observed for the LUMOs differs more significantly. Adding a chlorine atom (from 4CzIPN to 3CzClIPN) has a much weaker effect than adding a cyano group (from 4CzIPN to 5CzBN), resulting in a comparatively large HOMO-LUMO gap for 5CzBN while the gap for 4CzIPN and 3CzClIPN remains similar. This trend in the HOMO-LUMO gaps is closely related to the respective ΔE_{ST} of the molecules as the first singlet and triplet excited states are characterized by HOMO-to-LUMO transitions.

The photoluminescence (PL) (*cf.* Figure S14d, Supporting Information) and the EL response exhibit a strong correlation, suggesting that the molecules behave similarly under optical and electrical excitation. The corresponding CIE (*Commission internationale de l'éclairage*) chromaticity diagram is given in Figure 3d with the CIE values summarized in Table S2 (Supporting Information).

In the host–guest system, a distinct blue shift in the EL response is observed (*cf.* Figure S14c, Supporting Information). This shift is attributed to environmental changes induced by CBP, preventing aggregation-induced quenching, which can also lead to a blue shift in the EL response.[42] The reduced full width at half maximum (FWHM) values demonstrate the higher selectivity along with the more efficient light emission as interactions between the emitter molecules are decreased, which can be attributed to a modification of the energy transfer processes, e.g., Förster (FRET) and Dexter energy transfer (DET).[42,43] FRET mainly depends on the overlap of the PL spectrum of the host molecule and the absorption spectrum of the guest molecule.[16] As shown in **Figure** 4a, all TADF emitters exhibit a strong overlap with the PL spectrum of CBP, indicating efficient FRET between the host and guest molecules. This is corroborated by simulated time-dependent density functional theory (TD-DFT) absorption and PL spectra at the B3LYP-D3/def2-SVPD level of theory (see Figure S22, Supporting Information). From the UV–vis absorption spectra, we also determined the optical gap (ΔE_{opt}) using the Tauc plot method assuming a direct band gap.[44] The exact experimental values of ΔE_{opt} for the three molecules are presented

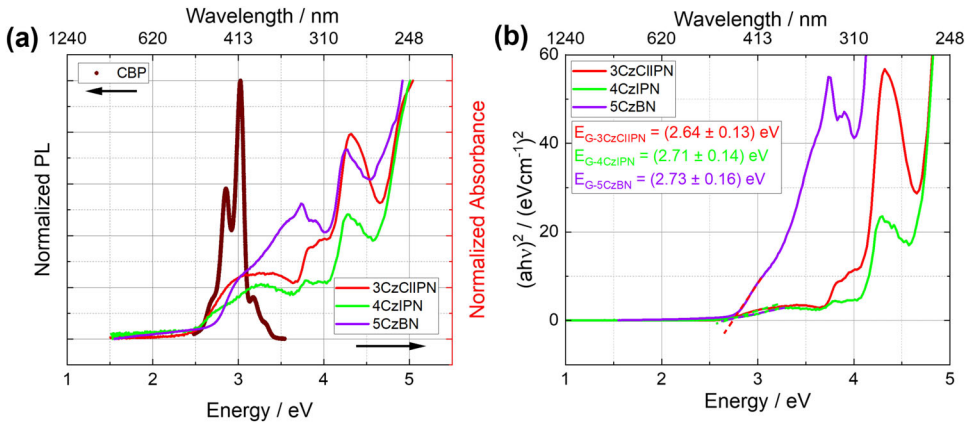

Figure 4. a) Absorbance spectra for the emitter molecules and PL spectra for the CBP host. The absorbance of all emitter materials overlaps with the PL of CBP, indicating an efficient FRET. b) Tauc plot with energy band gap for the bare emitter materials. ΔE_{opt} slightly increases with increasing number of carbazole units, which is well in line with the observed blue shift in the PL and EL response (vide supra).

in Figure 4b. These values correlate with the increasing HOMO–LUMO energy gap, and with the observed blue shift in the PL and EL responses correlated with the increasing number of carbazole units in the cyanoarene molecules.

Considering the external quantum efficiency (EQE) results in Figure 3c, the introduction of the host–guest system significantly enhances the EQE compared to the device consisting only of bare molecules. An increase in the EQE was detected when using a material with a smaller ΔE_{ST}, as the RISC process is more efficient. The EQE_{max} for 3CzClIPN and 4CzIPN is very similar, while 5CzBN shows a much lower EQE related to the larger ΔE_{ST}. The exact values for the optoelectronic characterization are summarized in Table S1 (Supporting Information). As mentioned, the increased EQE when comparing the host–guest system to the bare molecular systems can be attributed to better charge carrier transport according to an improved energy transfer, mostly originating from FRET (*cf.* Figure 4). Nevertheless, as the devices are not optimized, the total EQE values remain quite low. Due to the higher emitter concentration in the bare molecular devices, a concentration quenching effect is assumed. The lack of separation of emitter and transport functions in such layers favors exciton quenching.[45] As revealed by angular photoluminescence measurements, light outcoupling in the fabricated devices is limited due to predominantly vertical dipole orientation observed in neat molecular thin films. In contrast, the host–guest systems exhibit improved outcoupling, with an isotropic dipole distribution and a tendency toward horizontal alignment. The experimental results are presented in Figure S15 (Supporting Information), with the extracted vertical dipole orientation values shown in Figure S16a (Supporting Information) and the fitting error shown in Figure S16b (Supporting Information), respectively. The relatively high energy barriers (*cf.* Figure S13, Supporting Information) and the strong efficiency roll-off could be compensated in further investigations by improving the band alignment using additional transport and blocking layers.[46] However, the lower EQE positively impacts the MFE amplitude, as discussed in detail below.

Examining the calculated relative energy differences between the triplet energy levels of CBP and the excitonic TADF emitters reveals a difference of 0.22 eV for 3CzClIPN (*cf.* Figure S23a, Supporting Information), 0.16 eV for 4CzIPN (*cf.* **Figure 5**), and 0.02 eV for 5CzBN (*cf.* Figure S23b, Supporting Information). Since DET mainly depends on the alignment of the host and guest triplet states,[47] it should be most efficient for the combination of CBP and 5CzBN. However, the optoelectronic properties, and particularly the EQE, remain significantly higher for the other two TADF emitter molecules. This indicates that DET plays a less critical role in these devices compared to the intrinsic properties of the TADF emitter.

2.3. Characterization of Magnetic Field Effects

As discussed in section 2.2, the introduction of a host-guest system using CBP as the host matrix dramatically increased EQE (*cf.* Figure 3). In **Figure 6**, the organic magnetoconductance

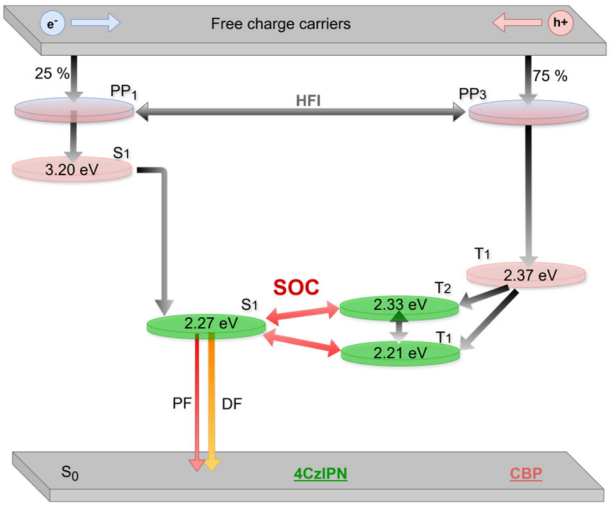

Figure 5. Jablonski diagram of 4CzIPN based on DFT and TD-DFT calculations (see Computational Details in the Supporting Information for a detailed breakdown of the computational methodology). Depicted is the energy alignment of 4CzIPN relative to the CBP matrix, with a focus on its application in a host-guest system.

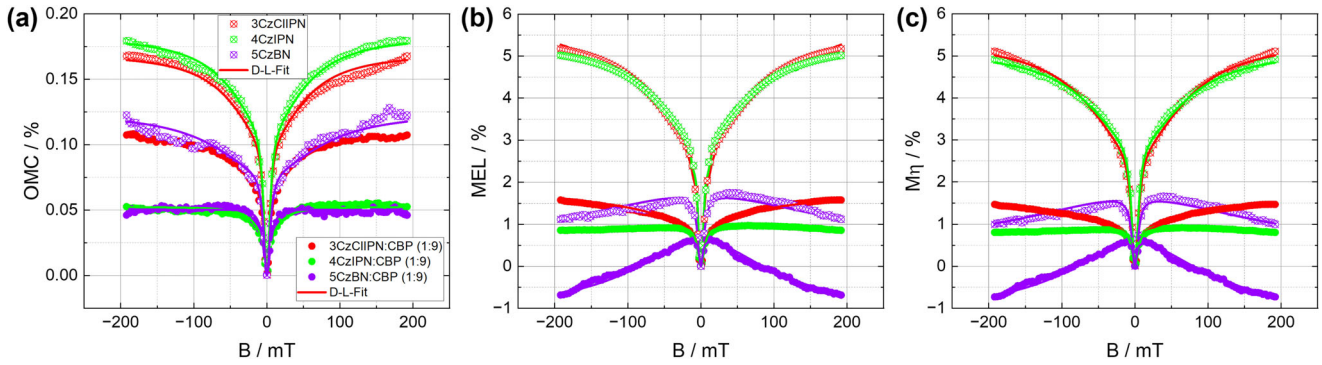

Figure 6. OMC (a), MEL (b), and M_η (c) detected at a constant current density of 175 mA cm^{-2} for the bare molecules and the host-guest system containing CBP as host matrix.

(OMC), magnetoelectroluminescence (MEL), and magnetoefficiency (M_η) responses of the bare molecular devices are compared to their respective host-guest equivalents as an example at a constant current density of 175 mA cm^{-2}. Since the OMC is less sensitive to radiative recombination and the MEL is affected by both radiative and non-radiative recombination, we propose the magneto-efficiency (M_η) as the most reliable metric. The relationship between the EL and the current (I) in OLEDs can generally be described by the formula EL = $\eta I/e$,[48] with η being the EL quantum efficiency and e the elementary charge. If η is B-dependent, the following relationship exists:[49]

$$M_\eta = \text{MEL} - \text{OMC} \tag{6}$$

The OMC signal was found to be quite low, which is in line with previous observations.[19,50] Interestingly, the opposite trend was observed when compared to the EQE analysis: The magnetic field effects are significantly quenched as device efficiency is improved. Niedermeier et al.[51] demonstrated that an electrical conditioning procedure could enhance the MFE response, which was associated with introducing trap states. As device efficiency increases, charge transport is also improved. Consequently, the interaction time of charge carriers with the external magnetic field is reduced, leading to a suppression of the MFE. Additionally, concentration quenching effects need to be considered[52] since the emitter concentration decreases by introducing a host-guest system, lowering the probability of interactions between the TADF emitters and the magnetic field.

In both cases, for the bare emitter devices and their host-guest systems, M_η is quenched upon increasing ΔE_{ST}. The MEL response of 5CzBN exhibits a markedly different line shape compared to those of the other two molecules. Thus, while improving EQE is certainly valuable, it would introduce additional complexity that would obscure the MFE response and reduce its magnitude. For the following analysis, we will focus on the bare molecular systems, as their measured MFE signals are stronger and hence more straightforward to analyze. To gain deeper insights, the OMC and MEL responses were measured at various current densities, as demonstrated in **Figure** 7 for the bare molecular devices. From left to right, the molecules exhibit an increasing ΔE_{ST}, which reduces the likelihood of RISC.[21] As expected, the MFE decreases accordingly, emphasizing its sensitivity to the RISC process. Interestingly however, the line shape does not replicate the characteristic fingerprint curves of the RISC process, which would typically correspond to a negative MEL response.[16,50]

For a more detailed analysis, the curves depicted in Figure 7 were fitted by a combination of two Lorentzian functions for the M_η response:

$$M_{\eta_{\text{fit}}}(\%) = \frac{MFE_{\text{LF}}B^2}{B^2 + B_{0-\text{LF}}^2} + \frac{MFE_{\text{HF}}B^2}{B^2 + B_{0-\text{HF}}^2} \tag{7}$$

with MFE_{LF} and MFE_{HF} corresponding to the amplitudes and $B_{0\text{-LF}}$ and $B_{0\text{-HF}}$ corresponding to the broadening of the curves (half width at half maximum - HWHM) for the low-field (LF) and high-field (HF), respectively. The two terms determine the major effects corresponding to the LF (<|20| mT), and HF effect regime (>20 mT). The broadening B_0 of the M_η response is also determined as the characteristic magnetic field. A comparison of several models (*cf.* Figure S18 and Tables S3 and S4, Supporting Information) showed that Equation (7) best replicates the M_η response. The error bars shown in the diagrams are derived from the standard deviation of ten separate measurements. Upon examination of the data presented in **Figure** 8, a decrease in the M_η response is observed with increasing ΔE_{ST}, which is well replicated in the MFE_{LF} variable in Figure 8(c).

Interestingly, the M_η response for 4CzIPN is slightly higher than that of 3CzClIPN, particularly at lower current densities (*cf.* Figure 8c). A comparison of the MFE results with the J–V and Luminance–V responses (*cf.* Figure S14a,b, Supporting Information) reveals that the variations in turn-on voltage (determined at 10 cdm^{-2}) and operational regimes are well reflected in the MFE responses, causing the different onset of the increasing MFE_{LF}. The high turn-on voltage observed for 3CzClIPN is attributed to a relatively large energy barrier, as evidenced by the band alignment (*cf.* Figure S13, Supporting Information). $B_{0\text{-LF}}$ exhibits values below 10 mT for all three emitter molecules, which was previously assigned to hyperfine-driven interaction between polaron pairs.[16,53] A decrease was observed with increasing ΔE_{ST}, suggesting an enhanced HFI as the acceptor strength increases and the number of carbazole units decreases. Additionally, a slight increase with rising current density was noted. We therefore attribute the detected LF effect, with $B_{0\text{-LF}} \approx 5 - 6$ mT, to hyperfine-induced spin state interconversion of the polaron pair species in 3CzClIPN and 4CzIPN.

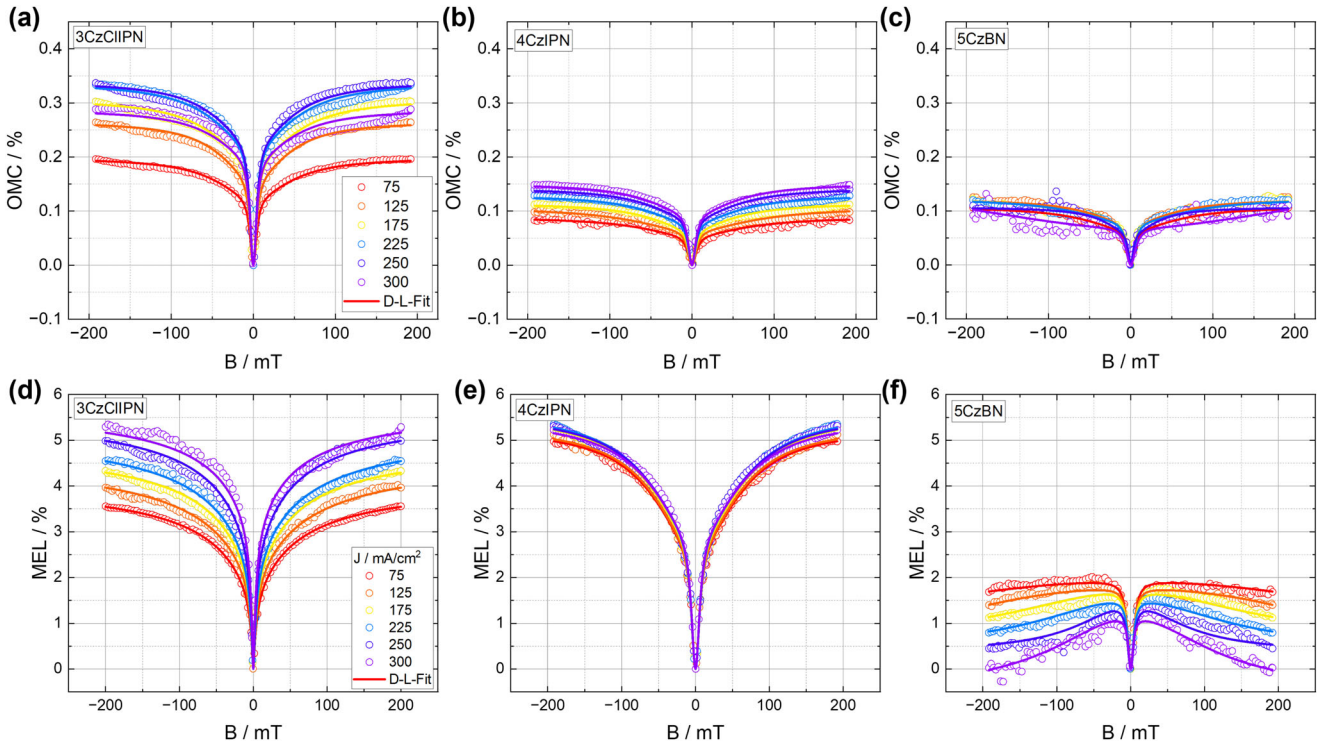

Figure 7. OMC (a–c) and MEL (d–f) detected at current densities from 75 mA cm^{-2} up to 300 mA cm^{-2} for the bare molecules 3CzClIPN (a) and (d), 4CzIPN (b) and (e), and 5CzBN (c) and (f).

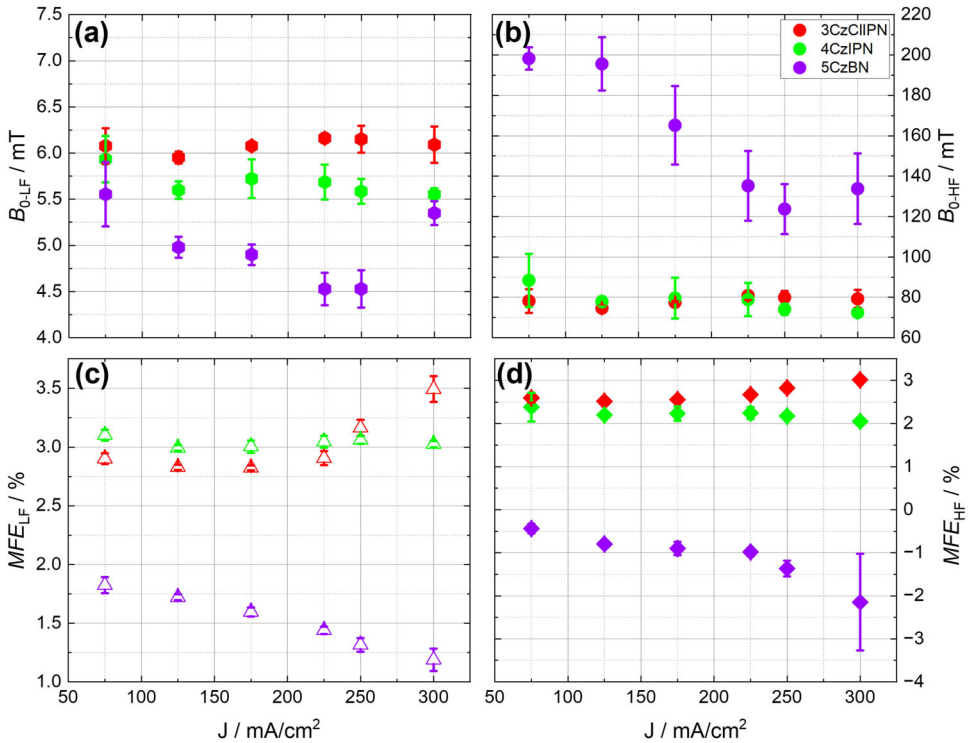

Figure 8. Fit analysis of the characteristic values obtained from the M_η curves in dependence of the current density for the three bare emitter molecular devices based on 3CzClIPN, 4CzIPN, and 5CzBN, respectively. The parameters obtained from the Double-Lorentzian fit defined in Equation (7) include the characteristic magnetic fields for the low- and high-field regimes, $B_{0\text{-LF}}$ and $B_{0\text{-HF}}$. Additionally, the amplitudes corresponding to these effects are represented by MFE_{LF} and MFE_{HF}, respectively.

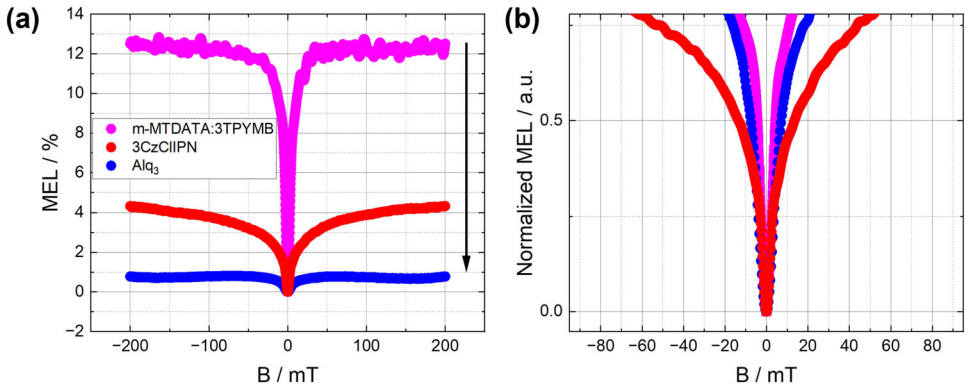

Figure 9. MEL detected at a constant current density of 175 mA cm^{-2} for 3CzIIPN (a) compared to the reference device with m-MTDATA:3TPYMB as a well-known exciplex system with dominant Δg and Alq_3 as a non-TADF emitter with the main spin state interconversion mechanism known to be hyperfine interaction. b) Normalized MEL response for the materials shown in (a) for better visibility of the difference in broadening.

For 5CzBN, a pronounced decrease in the broadening of $B_{0\text{-LF}}$ was observed. Since the characteristic magnetic field is directly proportional to the HFI, the decrease in HFI with increasing current density results in a significant drop in efficiency, as singlet polarons can no longer be harvested. This trend is further supported by the negative correlation of MFE_{LF}, as shown in Figure 8c. For 3CzClIPN and 4CzIPN, the amplitude of the effect increases with increasing current density (*cf.* MFE_{LF} and MFE_{HF}), revealing a positive low- and high-MFE. The MFE_{HF} behavior observed for 3CzClIPN and 4CzIPN is a clear indicator for triplet-charge annihilation.[17,50] The values extracted for $B_{0\text{-HF}}$ are in the range of 80 mT (*cf.* Figure S19a, Supporting Information), which are well in line with the characteristic magnetic field determined from spin-orbit coupling (SOC) calculated with TD-DFT (*cf.* Table S5, Supporting Information). By increasing ΔE_{ST}, the efficiency of the RISC dramatically decreases. For 5CzBN, which is exhibiting the highest ΔE_{ST}, even a slight negative trend for the $MFE_{LF/HF}$ upon applied current density was observed (*cf.* Figure 8c,d, Supporting Information). The results obtained for 5CzBN differ significantly from those observed for 3CzClIPN and 4CzIPN, especially for the MEL response (*cf.* Figure 7f, Supporting Information), which is further reflected in MFE_{HF} exhibiting negative values. Those are clear indicators of a dominant TTAmechanism.

Comparing our analysis to previous ones (e.g.,),[16,32] a noticeable discrepancy arises: The previous analysis employs a different fitting function, which separately determines the characteristic field of the RISC and TCA processes for the MEL response. However, from our perspective, this fitting function overfits the data. Furthermore, under an applied magnetic field, the TCA process is quenched, thereby enhancing the RISC process. This implies that TCA and RISC cannot be considered independent processes when TCA is present, as MFE measurements do not allow for their differentiation. This finding is further supported by the observed trend with increasing ΔE_{ST}, which must stem from changes in the efficiency of the RISC process. In the case of 5CzBN, the characteristic field for the HF effect is significantly higher compared to 3CzClIPN and 4CzIPN. Given the quenched MEL response at increased current density and the calculated characteristic magnetic field for SOC, the TCA process appears to play a minor role in this material system. For a deeper analysis of the model fit, we refer to the Supporting Information, especially to Figure S18 and Tables S3 and S4.

2.4. Evaluation of Spin Dynamics

To unravel the spin state interconversion process between the excitonic triplet and singlet states, we first fabricated reference devices with well-established properties. We examined Alq_3 as a non-TADF emitter[54] and a well-known exciplex-forming TADF system consisting of (4,4′,4″-Tris[phenyl(m-tolyl)amino]triphenylamine: Tris(2,4,6-trimethyl-3-(pyridin-3-yl)phenyl)borane (m-MTDATA:3TPYMB) at a donor-to-acceptor concentration ratio of 1:4.[19] In **Figure 9a**, the MEL response for the reference devices is compared to the one obtained for 3CzClIPN at a constant current density of J_{OLED} = 175 mA cm^{-2}. The absolute MEL at the highest applied magnetic field (B_{max} = 200 mT) differs. Alq_3 exhibits a lower absolute MEL response compared to m-MTDATA:3TPYMB and 3CzClIPN while the broadening of the curve is much more narrow compared to 3CzClIPN, as can be observed in the normalized plot in Figure 9b. The main spin state interconversion mechanism was previously attributed to hyperfine-induced spin-mixing of polaron pairs.[24,53] The MEL line shape observed for m-MTDATA:3TPYMB can be mainly attributed to the Δg mechanism as the dominant spin state interconversion process[16,19] while the broadening of the curve remains, as can be observed in the normalized plot in Figure 9b, similar to Alq_3. According to the spin state interconversion properties (the small ΔE_{ST} for exciplex materials and consequently the efficient RISC process), they are well known to exhibit a strong MEL response.[18,19,55] The small RISC activation energy, below the thermal energy at room temperature (≈ 25 meV), was identified as the primary cause of the pronounced magnetic field effects.[56]

In addition to the difference in the maximum MFE value, the broadening of the curve is different for 3CzClIPN. Even at high MFEs (≈200 mT), a saturation cannot be observed. Hence, the observed MFE response for the excitonic TADF emitter 3CzClIPN cannot be attributed to the already-mentioned mechanisms. The structural distinctions between the systems can partly explain this difference. In exciplex materials, the donor and acceptor

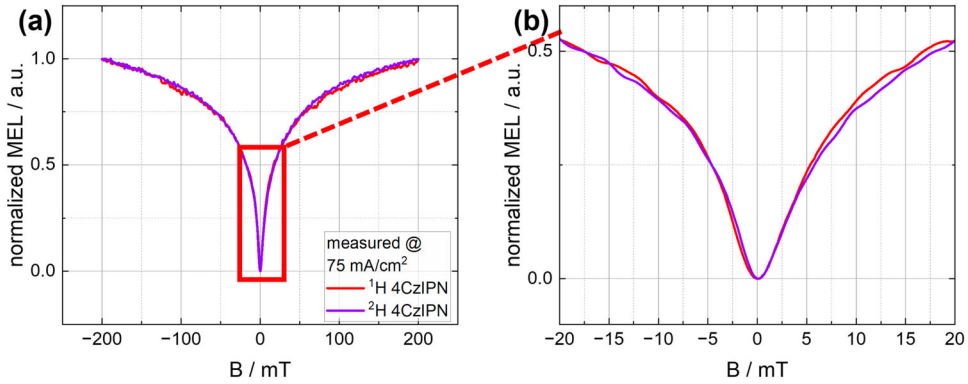

Figure 10. Panel (a) represents the normalized MEL response for the ^{1}H and ^{2}H isotopologues of 4CzIPN at a constant current density of 75 mA cm^{-2}, (b) shows the inset for the data obtained in (a) in the range from –20 to 20 mT. No difference in the broadening of the curves or the line shape could be observed.

units are located on separate molecules, leading to out-of-phase behavior in their Larmor frequencies under an external magnetic field.[19,24] Such behavior may disrupt the precision of spin alignment between PP_1 and PP_3, enhancing the MFE.[23,57] Alq_3 is not a TADF emitter, excluding the possibility of RISC and hence, of populating the S_1 state via the excited triplet states.

In contrast, excitonic TADF emitters are characterized by donor and acceptor units located on the same molecule. As a result, Δg-induced RISC can be ruled out as the dominant spin state interconversion mechanism for this system.[16] However, hyperfine-induced spin-mixing was previously reported in excitonic TADF emitters, as discussed above.

The key question remains whether the spin state interconversion for the excitonic bound electron–hole pairs (e-h) is driven by HFI or SOC. To address this, we compared the MEL response of all -^{1}H and all -^{2}H 4CzIPN isotopologues. Since the HFI is weaker in the deuterated molecules, a narrower MEL response is expected, as previously observed in studies on other molecular systems.[53] Interestingly, our results deviate from these prior findings, as no noticeable difference in curve broadening is observed (*cf.* **Figure 10**). Similar results were recently published by Liu et al.,[58] where a lack of an isotopic effect was found for TADF-OLEDs based on 4,6-Bis(3,5-di(pyridin-3-yl)phenyl)-2-methylpyrimidine (B3PymPm) at room temperature. Since variations in HFI are expected to influence the broadening of the MEL curve, the absence of such an effect suggests that HFI is not the dominant mechanism governing the MEL line shape. We therefore propose that the observed line shape is primarily determined by SOC, as reflected in the characteristic field $B_{0\text{-HF}}$ (vide supra). It is important to note that the interconversion of polaron pair spin states remains hyperfine-driven, as evidenced by the low-field feature $B_{0\text{-LF}}$ (*cf.* Figure 8a). While a detailed investigation of PP spin dynamics is beyond the scope of this work and has been addressed in previous studies, it is worth emphasizing that SOC-induced spin state interconversion within PP species is highly unlikely. This is because SOC is strongly dependent on the e-h pair separation, whereas HFI is not (*cf.* [59], Figure 5a of that work). Assuming HFI remains relatively constant with decreasing e-h distance, SOC increases significantly under such conditions. Consequently, for tightly bound excitonic e-h pairs, where SOC is orders of magnitude stronger than HFI, even subtle isotope effects on PP spin-mixing are likely masked by the dominant SOC-driven spin state interconversion processes occurring within the excitonic species.

Computational investigations support this hypothesis: The calculated SOC and hyperfine coupling (HFC) for 4CzIPN in T_1 equilibrium amount to 1.51×10^{-1} cm^{-1} and 5.00×10^{-4} cm^{-1}, respectively, indicating a much stronger interaction via SOC as it is three orders of magnitude larger than the HFC which mediates the HFI.

To further explore the SOC-mediated RISC mechanism, linear interpolated pathways (LIPs) between the equilibrium geometries of the involved excited states in 4CzIPN were constructed (**Figure 11**). LIPs model state transitions by interpolating from the initial to the final state along a reaction path traced in high-dimensional coordinates. This provides qualitative insights into the energy profiles along the path of interconversion and allows for the identification of relaxation and deactivation pathways.

Upon electrical excitation, the RISC mechanism is typically described as a spin state interconversion between the T_1 and S_1 states. However, the relatively large energy gap between T_1 and S_1 (81 meV, Figure 11a, left) suggests that, despite the strong SOC, this direct RISC mechanism is not as straightforward as initially thought unless secondary processes are involved. Additionally, the absence of direct crossings between these states further reduces the efficiency of potential RISC directly from the T_1 state. It should be noted, however, that this study does not explicitly include vibronic coupling, so RISC governed by a strong overlap of the vibrational wavefunctions in absence of a narrow ΔE_{ST} or crossing cannot formally be ruled out. However, a crossing between the T_2 and S_1 states is observed along the $T_2 - S_1$ relaxation pathway (Figure 11b) with a SOC of 1.05×10^{-1} cm^{-1} at the pictured crossing point. This suggests that the higher triplet state T_2 could serve as an intermediate in a possible additional RISC path.

This would first require an upconversion from the T_1 to the T_2 state before RISC could occur. Although the T_1 and T_2 states along the $T_1 - T_2$ pathway do not directly intersect (Figure 11c), a minimum energy conical intersection (MECI) between the T_1 and T_2 states could provide a potential route for upconversion as a prerequisite for the subsequent RISC to S_1. However, while PESs of different spin multiplicities cross along the whole one-dimensional hyperline, a true energy degeneracy between states

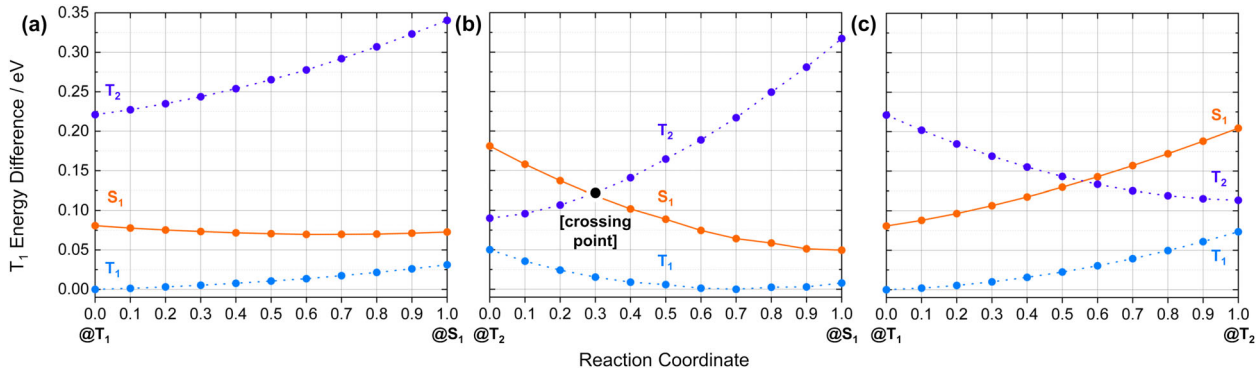

Figure 11. Excited state energies at LIPs between selected electronic state minima of 4CzIPN. Image (a) shows the $T_1 \rightarrow S_1$ LIP, (b) the $T_2 \rightarrow S_1$ LIP, and (c) the $T_1 \rightarrow T_2$ LIP. Dotted lines correspond to triplet PESs, while continuous lines represent the singlet state PES. All energies are relative to the energy of the T_1 state in its minimum.

of the same multiplicity is only achieved at a single point on the branching plane. This means that a 1D cutout of the PESs along one coordinate (such as a LIP) can pick up a singlet-triplet crossing with a higher likelihood than a triplet-triplet crossing. Therefore, a MECI between the T_1 and T_2 states might still exist even though it is not directly represented in the corresponding LIP. Consequently, a MECI search between the T_1 and T_2 states was performed using the branching plane updating gradient projection method by Maeda et al.[36] In addition to the MECI search, a minimum energy crossing point (MECP) search between the T_2 and S_1 states was conducted with the default gradient projection method by Bearpark et al.[35] The $T_2 - S_1$ pathway does already show a crossing between these states, but it might not yet represent a minimum along the corresponding hyperline. A second MECP search between the T_1 and S_1 states was also performed to ensure that no such intersection was overlooked in the LIP analysis. The combined insights of the MECI and MECP searches allow for a more detailed understanding of the interconversion mechanism, revealing key points that would otherwise be overlooked using just LIPs: Both a MECI between the T_1 and T_2 states and a MECP between the T_2 and S_1 states could be identified while the T_1 and S_1 states remained non-intersecting. Upon closer examination of the two identified crossing points, it became clear that the MECI is geometrically similar to a local minimum of the T_1 state (Root mean square deviation (RMSD) of 0.334 Å from the local minimum) while the MECP is in closer spatial proximity to the global minimum (RMSD of 0.017 Å from the global minimum). Consequently, if the $T_1 - T_2$ upconversion via the MECI occurs first, as mentioned above, a transition from the global to the local T_1 minimum will precede it. With this, a LIP spanning three distinct regions was constructed to provide a better overview of the overall interconversion mechanism (**Figure 12**). It shows the transition from the MECP to the global T_1 minimum, from the global to the local T_1 minimum, and from the local T_1 minimum to the MECI. An additional 2D LIP directly illustrating the region between the MECI and the MECP, provided for improved visualization of these points, is shown in Figure S24 of the Supporting Information.

Following the path laid out in Figure 12 and starting from the T_1 minimum (marked as 1 in Figure 12), a small energy barrier must be overcome first to move from the global minimum to the local minimum closer to the MECI (2). Once the T_2 state is populated via the MECI (3), an additional nearby crossing can be used to transition to the S_1 state (4). There, the molecule may again overcome a small energy barrier to reach the S_1 minimum. While the barrier separating global and local minima in the S_1 state is below 25 meV and therefore thermally accessible, the corresponding barrier in the T_1 state exceeds that limit, at least along the LIP reaction coordinate. However, global and local minima in both states are also connected by the displacement of a thermally active molecular normal mode (14.6 cm^{-1} in the the T_1 state and 13.2 cm^{-1} in the S_1 state, respectively) which can facilitate this transition. A similar connection was also suggested by Noda et al.[60]

Notably, geometry optimizations typically only reach the minimum closest to the initial guess structure and do not sample the respective conformational space. For complex systems with many degrees of freedom, this usually means that a multitude of MECPs and MECIs exist on the PESs, some potentially even lower in energy than the previously located minimum energy intersections. The described pathway could consequently be conceived as only one of many involving a T_2 intermediate.

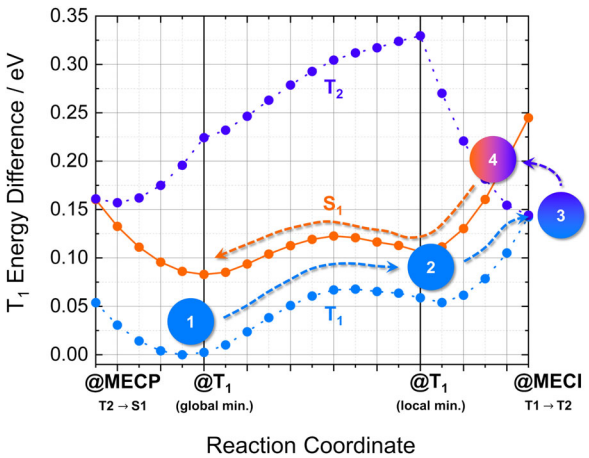

Figure 12. LIP between the $T_2 - S_1$ MECP, the global and local T_1 minima, and the $T_1 - T_2$ MECI. A T_2-mediated RISC pathway that passes a MECI and a MECP is indicated by arrows. All energies are relative to the energy of the T_1 state in its minimum.

Table 1. Spin-orbit and hyperfine coupling for 3CzClIPN, 4CzIPN, and 5CzBN in the respective electronic states. The SOC values extracted from the experimental data are shown for comparison.

Molecule	SOC electronic state	SOC_{comp} [cm^{-1}]	SOC_{exp} [cm^{-1}]	HFC electronic state	HFC_{comp} [cm^{-1}]
3CzClIPN	T_1	1.21×10^{-1}	–	T_1	5.66×10^{-4}
	$T_2 - S_1$ MECP	1.37×10^{-1}	$(1.46 \pm 0.04) \times 10^{-1}$	T_2	5.46×10^{-4}
4CzIPN	T_1	1.51×10^{-1}	–	T_1	5.00×10^{-4}
	$T_2 - S_1$ MECP	1.95×10^{-1}	$(1.46 \pm 0.10) \times 10^{-1}$	T_2	4.96×10^{-4}
5CzBN	T_1	6.90×10^{-1}	–	T_1	5.02×10^{-4}
	$T_2 - S_1$ MECP†	3.07×10^{-1}	$(2.96 \pm 0.61) \times 10^{-1}$	T_2	–

This analysis shows that the RISC interconversion process in 4CzIPN is more complex than initially expected and that future discussions of TADF emitter materials require more nuance, as ΔE_{ST} is not necessarily directly related or proportional to the RISC activation energy but can instead be attributed to two different potential interconversion pathways.

Similar considerations can also be made for 3CzClIPN and 5CzBN, with the respective results for SOC and HFC presented in **Table 1** and the LIPs shown in the Supporting Information (Figures S25 and S26, Supporting Information). Notably, if the T_2 state is involved in the interconversion process, the relevant SOC occurs at the $T_2 - S_1$ MECP. Since this point bears no special significance in the HFI regime, the corresponding coupling constants were calculated in T_2 equilibrium instead for comparison. Due to the complex excited state character of the T_2 state of 5CzBN, no equilibrium geometry or $T_2 - S_1$ MECP could be converged. Instead, the unoptimized crossing found in LIP analysis was taken as the closest approximation for the calculation of the SOC. This is indicated by a dagger in Table 1 and **Table 2**.

These findings suggest that SOC remains the primary mediator of spin state interconversion across all three molecules. The upward trend in SOC from 3CzClIPN to 5CzBN can be attributed to a corresponding decrease in the torsional angles separating donor and acceptor moieties. This relationship was observed and elucidated for other TADF emitters as well.[61–63] In the absence of additional interactions, a perpendicular orientation of 90° between donor and acceptor units is usually sterically favored. Such an arrangement results in strong HOMO–LUMO separation, leading to a pronounced charge transfer (CT) character in the first excited singlet and triplet states. However, excessive spatial separation reduces orbital overlap, thereby weakening SOC. Moreover, direct SOC is significantly diminished between CT states involving the same orbitals and consequently showing similar CT character. In 3CzClIPN, the carbazole donor units are positioned too far apart to interact significantly, resulting in average torsional angles of 89.8° and 82.6°, and leading to CT characters of 0.86 and 0.85 for the respective S_1 and T_1 transitions (A value of 1 would signify a perfectly charge separated state and a value of 0 a local excitation).[64] In contrast, when carbazole groups are placed in closer proximity, as they are in 4CzIPN, steric repulsion and stabilizing π interactions drive the average torsional angles down to 72.3° and 67.0° for the corresponding S_1 and T_1 states. These reduced angles lower CT character but enhance SOC (CT values are provided in Table S6 in the Supporting Information). This effect becomes more pronounced with an increasing number of carbazole units; the average torsional angles in the S_1 and T_1 configurations of 5CzBN are further reduced to 66.6° and 62.6°, respectively. A substantial contribution to the large SOC enhancement in 5CzBN relative to the other two cyanoarene derivatives is also the discrepancy in CT character between the S_1 and T_1 transitions (0.81 and 0.64, respectively).

The data further shows that in 3CzClIPN, spin state interconversion can also occur via a T_2 intermediate, given the high similarity in excited state energies, crossing points, and coupling constants compared to 4CzIPN. However, the extent to which both pathways are involved in the RISC process is likely to be different for each system and cannot be quantified without further investigations.

In contrast, 5CzBN exhibits significantly stronger SOC but maintains a large ΔE_{ST}, generally indicative of inefficient RISC between these states. However, in the absence of a converged T_2 equilibrium geometry or a confirmed $T_2 - S_1$ MECP, a definitive conclusion cannot yet be drawn, as the T_2-mediated mechanism discussed earlier is currently not computationally accessible. Additionally, as previously noted, TTA likely plays a dominant role in the spin state interconversion processes of 5CzBN as well.

To further assess the feasibility of the RISC process, a quantitative approach complementing this qualitative analysis was carried out. To this end, we determined the RISC activation energy using experimental and computational methods.

Table 2. Experimental and computational activation energies for 3CzClIPN, 4CzIPN, and 5CzBN.

Molecule	E_{act} (exp.) [meV]	E_{act} (comp.) [meV]
3CzClIPN	(86.2 ± 4.3)	24.6 ($T_1 - S_1$)
		101.4 ($T_1 - T_2 - S_1$)
4CzIPN	(138.9 ± 6.9)	74.2 ($T_1 - S_1$)
		160.0 ($T_1 - T_2 - S_1$)
5CzBN	–	99.6 ($T_1 - S_1$)
		127.9 ($T_1 - T_2 - S_1$)†

2.5. Determination and Interpretation of Activation Energies in TADF Emitters

Temperature-dependent MFE measurements were conducted to determine the activation energy associated with RISC for various TADF emitters. The corresponding data for the OMC response

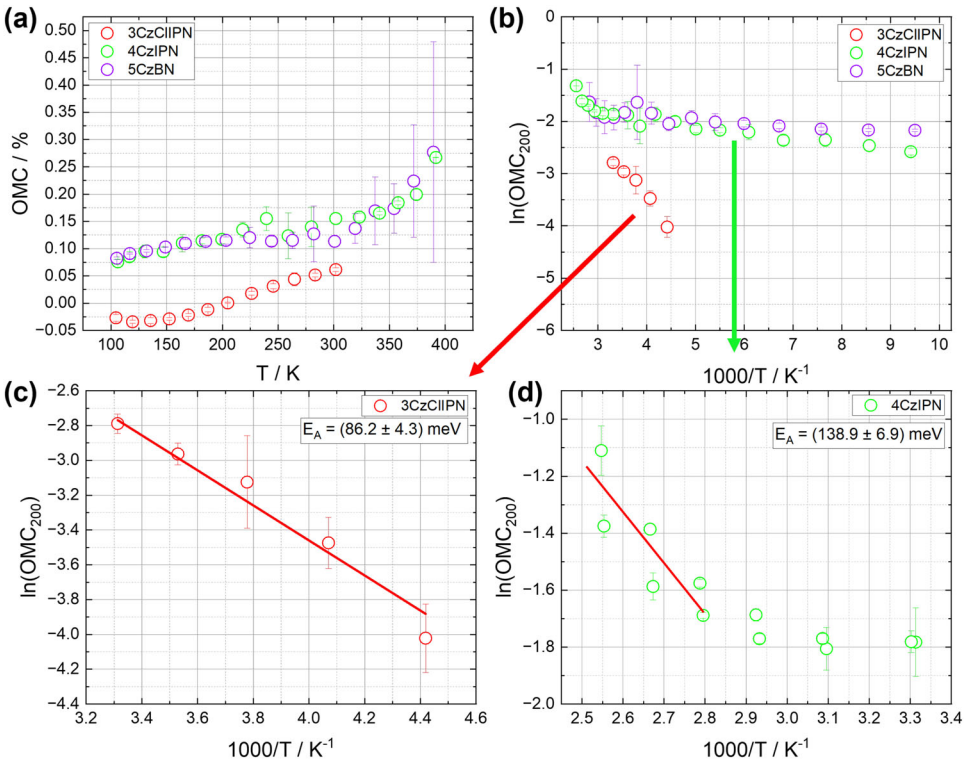

Figure 13. a,b) The temperature dependence observed for the OMC signal plotted over temperature (a) and the ln(OMC) over 1000/T (b) for 3CzClIPN, 4CzIPN, and 5CzBN, respectively. c,d) The respective Arrhenius plots with the values extracted from (b) for 3CzClIPN and 4CzIPN, respectively. The activation energy was determined by the strongest onset in the OMC response.

at a constant current density of $J_{OLED} = 175\,mA\,cm^{-2}$ is shown in **Figure 13**. The temperature dependence was fitted using the following expression:

$$MFE \propto exp\left(-\frac{E_{act}}{k_B T}\right) \quad (8)$$

where E_{act} denotes the activation energy, k_B the Boltzman constant, and T the temperature.[56] The complete MFE responses for both OMC and MEL are presented in Figure S20. A distinct difference between the temperature-dependent trends of the OMC and MEL responses was observed. Activation energies derived from the MEL response consistently fall below ΔE_{ST}, contradicting Marcus theory.[21,65] Despite this, previous studies by Liu et al.[58] and Basel et al.[18] extracted RISC activation energies from MEL data, reporting values significantly lower than the thermal energy at room temperature. Given that the reorganization energy is expected to be on the order of several tens of meV,[21] these discrepancies likely result from competing loss mechanisms.

In this work, we extracted the activation energy from the temperature-dependent OMC response (*cf.* Figure 13). For 3CzClIPN, a sign change in the OMC response was observed, with negative values appearing at low temperatures (*cf.* Figure S20a, Supporting Information). This behavior has previously been attributed to the onset of bipolar transport being temperature dependent, where at low temperatures only one type of charge carrier dominates the charge transport.[66] From the Arrhenius plots in Figure 13c,d, the activation energy was determined to be (86.2 ± 4.3) meV for 3CzClIPN and (138.9 ± 6.9) meV for 4CzIPN (*cf.* Table 2). It can further be observed from panels (c) and (d) that the onset of a significant OMC response shifts to higher temperatures with increasing activation energy.

Interestingly, no activation energy could be extracted for 5CzBN. As discussed previously, its MFE response is predominantly governed by hyperfine-induced spin-mixing of polaron pairs (visible in the LF effect regime) and TTA (dominating the HF effect regime). Therefore, the temperature dependence does not reflect the RISC process alone. Moreover, the activation energy is likely too high to be reliably measured within the accessible temperature range. Upon increasing the temperature, structural degradation, most likely within the emissive layer, was observed, compromising the measurement reliability. This is reflected in the large error bars in Figure 13a. Additionally, a poor signal-to-noise ratio, as illustrated in Figure S21 (Supporting Information), further hindered reliable analysis.

Computationally, the energy barrier that must be overcome to drive the RISC process via the T_2-mediated pathway can be described as the energy difference between T_1 equilibrium and the $T_2 - S_1$ MECP.[21] For the direct $T_1 - S_1$ pathway, an activation energy can be estimated from the following Marcus Theory-like expression incorporating ΔE_{ST}:[65]

$$E_{act} = \frac{(\Delta E_{ST} + \lambda)^2}{4\lambda} \quad (9)$$

where λ is the reorganization energy. The results for both pathways are summarized in Table 2.

Even though the computationally and experimentally determined activation energies seem to align better with the idea of a dominant T_2-mediated pathway, a noticeable discrepancy between both sets of values is apparent. From our perspective, this difference can be attributed to processes such as non-radiative recombination and the need to overcome energy barriers resulting from the simplified layer stack. Additionally, as discussed above, the MFE responses are influenced not only by RISC but also by triplet-related processes. Our computational modeling does not include the influence of these effects on the activation energy of the RISC, limiting direct comparability. Conversely, the activation energy derived from MFE measurements reflects a superposition of various effects, making it impossible to isolate the RISC activation energy alone. In the cases of 3CzClIPN and 4CzIPN, the observed activation energy likely consists of contributions from both TCA and RISC, as well as additional energy required to overcome interfacial energy barriers due to imperfections in the layer stack and energy level alignment.

Consequently, no decisive conclusion regarding the dominance of one RISC pathway over the other should be drawn from this comparison alone.

3. Conclusion

Throughout this study, we compared three cyanoarene-type molecules with different singlet–triplet energy gaps (ΔE_{ST}). By combining experimental and computational approaches, we found that the interconversion between triplet and singlet excited states of excitonically bound electron–hole pairs is predominantly driven by spin–orbit coupling rather than hyperfine interactions.

Furthermore, the reverse intersystem crossing process in these molecules can also occur via the T_2 state in addition to the direct $T_1 - S_1$ pathway. This indicates that it is not directly influenced by the ΔE_{ST} between T_1 and S_1 states, but instead by the respective activation energies of the different pathways and the dynamics associated with the spin state interconversion mechanism.

A comparison between 3CzClIPN, 4CzIPN, and 5CzBN also revealed significant differences in charge transport properties. Charge transport in 5CzBN was primarily dominated by triplet-triplet annihilation, resulting in an inefficient RISC process. Triplet-charge annihilation is the primary mechanism in the other two molecules, contributing to the RISC process under applied magnetic field. These findings demonstrate that the application of an external magnetic field is a powerful and non-destructive tool to investigate charge transport properties.

Using a Double-Lorentzian model to fit the magnetic field effect response, we successfully replicated the measured data without overfitting. This approach also revealed that distinguishing between the reverse intersystem crossing and triplet-charge annihilation processes is not possible in the presence of a magnetic field, and that they are inherently linked.

The dynamics of triplet-triplet annihilation as a competitive spin state interconversion mechanism in 5CzBN require a broader computational investigation that accounts for the complex thin film environment to complement our initial experimental findings. Given the vast diversity of cyanoarene emitters, our results could be compared with those of other molecules available from either our own synthetic toolbox[67] or from promising new approaches for similar TADF emitters[68,69] to identify broader trends. Especially the influence of different donor groups, e.g., diphenylamine-containing cyanoarene molecules, would be of great interest.

This work unravels the spin state interconversion and the dominant charge transport properties of carbazole-containing cyanoarene TADF emitters and paves the way for the development of efficient spintronic devices.

4. Experimental Section

Materials: As substrates, pre-patterned indium tin oxide (ITO) glass substrates provided by Ossila were used. Poly-(3,4-ethylendioxythiophene)-poly-(styrene sulfonate) (PEDOT:PSS) was purchased from Heraeus (Clevios^{TM}—PEDOT:PSS). Additionally, molybdenum(VI) oxide powder (MoO_3) and lithium fluoride (LiF) were purchased from Sigma-Aldrich. 2,4,6-Tri(9*H*-carbazol-9-yl)-5-chloroisophthalonitrile (**3CzClIPN**), and Penta-carbazolylbenzonitrile (**5CzBN**) were synthesized by Tom Gabler. 2,4,5,6-Tetra-9*H*-carbazol-9-yl (**4CzIPN**) was purchased from Angene. 4,4′-Bis(9*H*-carbazol-9-yl)biphenyl (**CBP**) was purchased from TCI chemicals. 2,2′,2″-(1,3,5-Benzinetriyl)-tris(1-phenyl-1-*H*-benzimidazole) (TPBi) was purchased from Ossila. All materials were used without further purification. The PEDOT:PSS solution was diluted with isopropanol (IPA) at a ratio of 1: 0.04 w%. MoO_3 was mixed with PEDOT:PSS at a ratio of 0.02: 1. Prior to this, the MoO_3 powder was dissolved in ammonium hydroxide (NH_3OH) (0.25 g/ml). The initial solutions for 4CzIPN, 3CzClIPN, and 5CzBN as well as for CBP were prepared to be 20 mg/ml in toluene. The two solutions were mixed afterward at a mass ratio of 9: 1 for the CBP:TADF emitters. Prior to device fabrication, all solutions were treated in an ultrasonic bath at 80 °C for at least 30 min. and filtered through a nylon syringe with a pore size of 0.22 µm. The remaining materials were deposited via thermal evaporation.

Experimental Details: The TADF devices were fabricated with the following structure (*cf.* Figure 1a,b: ITO (115 nm, purchased by Ossila, pre-patterned cathode (eight pixels)/ PEDOT:PSS + MoO_3 (35 nm)/ bare TADF emitter (≈30nm)/ TPBi (20 nm)/ LiF (0.8 nm)/ Al (110 nm). The thickness of the spin-coated layer was measured using profilometry, with an associated thickness variation of 8%. Before the PEDOT:PSS + MoO_3 was deposited, the samples were cleaned with alkaline detergent + DI water and IPA in an ultrasonic bath for 30 min., respectively. Afterward, the samples were dried with nitrogen. The surface was further activated by a UV-Ozon treatment with a custom-built setup (after)[70] for 35 min. All solutions were spin-coated at 3000 rpm (acceleration 300 rpm s^{-1}) for 30 s and post-annealed at 80 °C for 30 min. TPBi was evaporated at constant rates of 1 Å s^{-1}. LiF and Al were evaporated at constant rates of 0.1 and 5 Å s^{-1}, respectively. The deposition via thermal evaporation in the vacuum chamber was performed at a pressure of 10^{-6} mbar. The devices were encapsulated with epoxy resin and a glass slide, followed by post-treatment under a UV lamp for 15 min. For a detailed description of the measurement setup, refer to the Supporting Information, section S1.1. The hardware and software are explained in detail, and the software Python code can be found on GitHub: https://github.com/semiconductor-physics/Organic-MFE-Measurement. The PL spectrum was recorded by a Jasco CD spectrometer, where the excitation wavelength was chosen to be λ_{ex} = 405 nm for 3CzClIPN and 4CzIPN, while the excitation wavelength was chosen to be λ_{ex} = 370 nm for 5CzBN. The UV-vis absorption spectra were measured using a Cary 60 UV-vis spectrometer. The baseline was determined using quartz glass and subtracted from the spectra of interest. To perform photometric characterization of

the fabricated OLEDs, a Gigahertz-Optik UMBK-150 integrating sphere (sphere diameter of 150 mm) was utilized to detect all the emitted light. The electrical control and measurement of the OLEDs were carried out using a Keithley 2636B SourceMeter. The photocurrent output of the integrating sphere was converted into a voltage via an amplifier and detected by an Agilent 34411A multimeter. The entire measurement setup was controlled automatically using a LabVIEW program, recording the *I–V* curve of the OLEDs and measuring light current, optical power, and EQE as a function of voltage. Angular photoluminescence measurements were conducted using the Phelos system from Fluxim, employing a 365 nm excitation provided by a photodiode. Substrate microscopy glass slides were used and films were produced with the same parameters as the emitter films for the OLED devices. The PL quantum yield measurements were performed with the Edinburgh Instruments FLS1000 photoluminescence spectrometer. For excitation in the integrating sphere, a Xe lamp was used with an excitation wavelength of 405 nm. The spectra were recorded in the range of 320 − 800 nm using the PMT-980 detector. The ionization energies *IE* and electron affinities *EA* of 3CzClIPN, 4CzIPN, and 5CzBN corresponding to their HOMO and LUMO onsets, as well as the work function *W* of 4CzIPN were determined experimentally by the combination of ultraviolet photoemission spectroscopy (UPS) and low-energy inverse photoemission spectroscopy (LEIPES). Both experiments were combined in the same analysis chamber of an ultra-high vacuum (UHV) setup with a base pressure of 1×10^{-10} mbar. The techniques were applied to thin films of 3CzClIPN, 4CzIPN, and 5CzBN thermally evaporated on Si substrates with a 100 nm thick Au layer on top in a connected preparation chamber. The substrates were prepared by successive sonication in acetone, ethanol and DI water before loading them into the UHV chamber. Thermal evaporation of 4CzIPN was carried out successively in five steps to achieve five different film thicknesses to identify possible interfacial effects of energy band alignment and determine at which thickness bulk-like conditions are achieved. For the other molecules, only two layers were deposited, every second one in the likely range of bulk-like conditions. The evaporation rate was controlled using a quartz crystal microbalance (QCM), and resulting thickness values and chemical purity of the organic films were confirmed using X-ray photoemission spectroscopy (XPS). For UPS, the He I emission line from a He-discharge lamp was used. XPS was carried out using the unmonochromated AlKα line from a XR50 X-ray source by SPECS. The photoemission signal in both cases was detected using a PHOIBOS 150 hemispherical analyzer in combination with a 1D delay-line detector, also by SPECS. For LEIPES, a custom-built setup, designed after,[71] was used, including a custom-built electron source designed after[72] with a BaO cathode by Kimball Physics, and a photodetection system using the R2078 photomultiplier by HAMAMATSU. LEIPES measurements were carried out in the isochromat mode, using a variety of Bragg filters purchased from Edmund Optics and Laser Components Germany as optical bandpass. The central wavelengths of the used filters were 250, 260, 266, and 270 nm, all with a FWHM of 10 nm. The spectral resolution of the LEIPES setup was determined to be 0.3 eV via the spectral broadening of the Fermi edge of a clean polycrystalline Ag substrate. The same procedure resulted in a spectral resolution of 110 meV for UPS. Measurement of the FWHM of the Ag3d core levels yielded a spectral resolution of 1.3 eV for XPS.

Computational Details: Ground and excited state geometries were optimized using B3LYP-D3/6-31+G* with Gaussian 16,[73] according to the level of theory validated in a prior TADF study.[74] The S_1, T_1, and T_2 states were optimized with TD-DFT following conformational sampling of the ground state via GOAT[75] and the GFN2-XTB method. Minimum energy crossing points (MECPs) and conical intersections (MECIs) were located using a gradient projection and a modified gradient projection algorithm (branching plane updating) implemented in the KST48 program[76,77] and interfaced with Orca 5.0.4[78,79] at the B3LYP-D3/def2-SVPD level of theory with TD-DFT. Electronic properties (energies, spin-orbit couplings, hyperfine couplings) were computed at the same level of theory in Orca 6.0.1. Charge transfer (CT) character was analyzed with TheoDORE 3.2.[64,80]

A detailed breakdown of the computational methodology can be found in the Supporting Information.

Supporting Information

Supporting Information is available from the Wiley Online Library or from the author.

Acknowledgements

A.M. and J.W. contributed equally to this work. The authors would like to acknowledge Jörn Langenickel for the possibility to use the optoelectronic measurement setup. The authors thank Prof. Dr. Michael Mehring for the possibility to use the UV–vis spectrometer. Further, the authors would like to thank Prof. Dr. Simon Kahmann for the opportunity to use his angular PL spectrometer "Phelos" from Fluxim. A.M. and G.S. would like to thank SAB for funding this research under the project number 100649391 (ReSIDA-H2). The authors gratefully acknowledge funding by the Deutsche Forschungsgemeinschaft (DFG, German Research Foundation) through DFG-TRR 386-B03/B05/B06/B08 (514664767) as well as the resources on the LiCCA HPC cluster of the University of Augsburg, co-funded by the DFG – Project-ID 499211671. D.R.T.Z. and A.E. would like to thank the DFG for funding (Research Unit FOR 5387 POPULAR, project no. 461909888). The work of C. D. and D. B. was co-financed by the European Union and by tax funds in accordance with the budget adopted by the Saxon state parliament (EFRE InfraProNet 2021-2027 NachLeuchten 100701886 and 100701890).

Conflict of Interest

The authors declare no conflict of interest.

Data Availability Statement

The software developed for the organic magnetic field effect measurement setup can be found on GitHub: https://github.com/semiconductor-physics/Organic-MFE-Measurement Additional data supporting the findings described in the manuscript can be found in the Supporting Information. The full data is available upon reasonable request from the corresponding author.

Keywords

cyanoarenes, magnetic field effects (MFE), reverse intersystem crossing (RISC), spin-orbit coupling (SOC), thermally activated delayed fluorescence (TADF)

Received: May 12, 2025
Revised: August 5, 2025
Published online:

[1] G. Hong, X. Gan, C. Leonhardt, Z. Zhang, J. Seibert, J. Busch, S. Bräse, *Adv. Mater.* **2021**, *33*, 2005630.
[2] J. Dos Santos, D. Hall, B. Basumatary, M. Bryden, D. Chen, P. Choudhary, T. Comerford, E. Crovini, A. Danos, J. De, S. Diesing, M. Fatahi, M. Griffin, A. Kumar Gupta, H. Hafeez, L. Hämmerling, E. Hanover, J. Haug, T. Heil, D. Karthik, S. Kumar, O. Lee, H. Li, F. Lucas, C. Frank Ross Mackenzie, A. Mariko, T. Matulaitis, F. Millward, Y. Olivier, Q. Q. D. W. Samuel, et al., *Chem. Rev.* **2024**, *124*, 13736.
[3] D. Yin, J. Feng, R. Ma, Y.-F. Liu, Y.-L. Zhang, X.-L. Zhang, Y.-G. Bi, Q.-D. Chen, H.-B. Sun, *Nat. Commun.* **2016**, *7*, 11573.
[4] W. Kim, S. Kwon, S.-M. Lee, J. Kim, Y. Han, E. Kim, K. C. Choi, S. Park, B.-C. Park, *Org. Electron.* **2013**, *14*, 3007.

[5] S. Kwon, H. Kim, S. Choi, E. Jeong, S. Kim, D.and Lee, H. Lee, Y. Seo, K. Choi, *Nano Lett.* **2018**, *18*, 347.
[6] J. Song, H. Lee, E. Jeong, K. Choi, S. Yoo, *Adv. Mater.* **2020**, *32*, 1907539.
[7] M. Hauck, C. Bickmann, A. Morgenstern, N. Nagel, C. Meinecke, A. Schade, R. Tafat, L. Viriato, H. Kuhn, G. Salvan, D. Schondelmaier, T. Ullrich, T. von Unwerth, S. Streif, *Energies* **2024**, *17*, 20.
[8] K. Cole, R. Cole, *J. Chem. Phys.* **1941**, *9*, 341.
[9] H. Wang, Y. Yuan, Z. Wang, Y. Wang, *ACS Appl. Eng. Mater.* **2024**, *2*, 781.
[10] C. Adachi, M. Baldo, M. Thompson, S. Forrest, *Jpn. J. Appl. Phys.* **2001**, *90*, 5048.
[11] C. Adachi, *Jpn. J. Appl. Phys.* **2014**, *53*, 060101.
[12] H. Nakanotani, Y. Tsuchiya, C. Adachi, *Chem. Lett.* **2021**, *50*, 938.
[13] H. Uoyama, K. Goushi, K. Shizu, H. Nomura, C. Adachi, *Nature* **2012**, *492*, 234.
[14] K. Shizu, M. Uejima, H. Nomura, T. Sato, K. Tanaka, H. Kaji, C. Adachi, *Phys. Rev. Appl.* **2015**, *3*, 014001.
[15] N. Kotadiya, P. Blom, G.-J. A. Wetzelaer, *Nat. Photonics* **2019**, *13*, 765.
[16] Z. Wang, X. Jiang, J. Xiong, B. Xiao, Y. Wang, X. Zhou, R. Pan, X. Tang, *J. Phys. Chem. Lett.* **2024**, *15*, 9630.
[17] M. Tanaka, R. Nagata, H. Nakanotani, C. Adachi, *Commun. Mater.* **2020**, *1*, 18.
[18] T. Basel, D. Sun, S. Baniya, R. McLaughlin, H. Choi, O. Kwon, Z. Vardeny, *Adv. Electron. Mater.* **2016**, *2*, 1500248.
[19] Y. Wang, K. Sahin-Tiras, N. Harmon, M. Wohlgenannt, M. Flatté, *Phys. Rev. X* **2016**, *6*, 011011.
[20] J. Gibson, A. Monkman, T. Penfold, *ChemPhysChem* **2016**, *17*, 2956.
[21] N. Aizawa, Y. Harabuchi, S. Maeda, Y.-J. Pu, *Nat. Commun.* **2020**, *11*, 3909.
[22] X. Pan, O. Kwon, D. Khanal, B. Choi, Z. V. Vardeny, *Adv. Opt. Mater.* **2022**, *10*, 2101334.
[23] A. Mondal, X. Pan, Z. Kwon, O.and Vardeny, *ACS Appl. Mater. Interfaces* **2023**, *15*, 9697.
[24] A. J. Schellekens, Master's thesis, Eindhoven University of Technology, Eindhoven, Netherlands, **2010**.
[25] A. Morgenstern, D. Weber, L. Hertling, K. Gabel, U. Schwarz, D. Schondelmaier, D. R. T. Zahn, G. Salvan, *Sci. Rep.* **2024**, *14*, 30520.
[26] D. Weber, A. Morgenstern, D. Beer, D. R. T. Zahn, C. Deibel, G. Salvan, D. Schondelmaier, *Appl. Phys. A* **2024**, *130*, 1.
[27] R. Geng, R. Subedi, H. Luong, M. Pham, W. Huang, X. Li, K. Hong, M. Shao, K. Xiao, L. Hornak, T. D. Nguyen, *Phys. Rev. Lett.* **2018**, *120*, 086602.
[28] S. Crooker, F. Liu, M. Kelley, N. Martinez, W. Nie, A. Mohite, I. Nayyar, S. Tretiak, D. Smith, P. Ruden, *Appl. Phys. Lett.* **2014**, *105*, 15.
[29] E. Ehrenfreund, Z. Vardeny, *Isr. J. Chem.* **2012**, *52*, 552.
[30] T. Nguyen, G. Hukic-Markosian, F. Wang, L. Wojcik, X.-G. Li, E. Ehrenfreund, Z. Vardeny, *Nat. Mater.* **2010**, *9*, 345.
[31] Y. Hu, X. Tang, R. Pan, J. Deng, H. Zhu, Z. Xiong, *Phys. Chem. Chem. Phys.* **2019**, *21*, 17673.
[32] X. Zhao, J. Chen, L. Cheng, S. Yang, B. Wang, T. Peng, J. Liu, H. Lu, S. Zhang, Z. Xiong, *ACS Photonics* **2023**, *11*, 230.
[33] T. Ogiwara, Y. Wakikawa, T. Ikoma, *J. Phys. Chem. A* **2015**, *119*, 3415.
[34] S. Mukherjee, D. Fedorov, S. Varganov, *Annu. Rev. Phys. Chem.* **2021**, *72*, 515.
[35] M. Bearpark, M. Robb, H. Schlegel, *Chem. Phys. Lett.* **1994**, *223*, 269.
[36] S. Maeda, K. Ohno, K. Morokuma, *J. Chem. Theory Comput.* **2010**, *6*, 1538.
[37] S. Matsika, P. Krause, *Annu. Rev. Phys. Chem.* **2011**, *62*, 621.
[38] E. Bassan, R. Inoue, D. Fabry, F. Calogero, S. Potenti, A. Gualandi, P. Cozzi, Kamogawa, P. Ceroni, Y. Tamaki, O. Ishitani, et al., *Sustainable Energy Fuels* **2023**, *7*, 3454.
[39] M. Uda, A. Nakamura, T. Yamamoto, Y. Fujimoto, *J. Electron Spectrosc. Relat. Phenom.* **1998**, *88*, 643.
[40] F. Flores, J. Ortega, H. Vázquez, *Phys. Chem. Chem. Phys.* **2009**, *11*, 8658.
[41] A. Sugie, K. Nakano, K. Tajima, I. Osaka, H. Yoshida, *J. Phys. Chem. Lett.* **2023**, *14*, 11412.
[42] K. Stavrou, L. Franca, A. Monkman, *ACS Appl. Electron. Mater.* **2020**, *2*, 2868.
[43] B. Karunathilaka, U. Balijapalli, C. Senevirathne, S. Yoshida, Y. Esaki, K. Goushi, T. Matsushima, A. Sandanayaka, C. Adachi, *Nat. Commun.* **2020**, *11*, 4926.
[44] B. Viezbicke, S. Patel, B. Davis, D. Birnie III, *Phys. Status Solidi B* **2015**, *252*, 1700.
[45] Y. Zhang, Z. Li, C. Li, Y. Wang, *Front. Chem.* **2019**, *7*, 302.
[46] H. Nakanotani, K. Masui, J. Nishide, T. Shibata, C. Adachi, *Sci. Rep.* **2013**, *3*, 2127.
[47] J. Kim, S. You, N. Kim, J.-A. Yoon, K. Cheah, F. Zhu, W. Kim, *Sci. Rep.* **2014**, *4*, 7009.
[48] Y. Zhang, R. Liu, Y. Lei, Z. Xiong, *Appl. Phys. Lett.* **2009**, *94*, 8.
[49] R. Pan, X. Tang, Y. Hu, H. Zhu, J. Deng, Z. Xiong, *J. Mater. Chem. C* **2019**, *7*, 2421.
[50] F. Wu, X. Zhao, H. Zhu, X. Tang, Y. Ning, J. Chen, X. Chen, Z. Xiong, *ACS Photonics* **2022**, *9*, 2713.
[51] U. Niedermeier, M. Vieth, R. Pätzold, W. Sarfert, H. Von Seggern, *Appl. Phys. Lett.* **2008**, *92*, 19.
[52] H. Kim, S.-R. Park, M. Suh, *J. Phys. Chem. C* **2017**, *121*, 13986.
[53] T. Nguyen, T. Basel, Y.-J. Pu, X. Li, E. Ehrenfreund, Z. Vardeny, *Phys. Rev. B: Condens. Matter Mater. Phys.* **2012**, *85*, 245437.
[54] J. Kalinowski, M. Cocchi, D. Virgili, P. Di M., V. Fattori, *Chem. Phys. Lett.* **2003**, *380*, 710.
[55] Y. Lei, Q. Zhang, L. Chen, Y. Ling, P. Chen, Q. Song, Z. Xiong, *Adv. Opt. Mater.* **2016**, *4*, 694.
[56] Y. Ling, Y. Lei, Q. Zhang, L. Chen, Q. Song, Z. Xiong, *Appl. Phys. Lett.* **2015**, *107*, 21.
[57] C. Zhang, D. Sun, C. Sheng, Y. Zhai, K. Mielczarek, A. Zakhidov, Z. Vardeny, *Nat. Phys.* **2015**, *11*, 427.
[58] X. Liu, H. Popli, O. Kwon, H. Malissa, X. Pan, B. Park, B. Choi, S. Kim, E. Ehrenfreund, C. Boehme, Z. V. Vardeny, *Adv. Mater.* **2020**, *32*, 2004421.
[59] B. Hu, L. Yan, M. Shao, *Adv. Mater.* **2009**, *21*, 1500.
[60] H. Noda, X.-K. Chen, H. Nakanotani, T. Hosokai, M. Miyajima, N. Notsuka, Y. Kashima, J.-L. Brédas, C. Adachi, *Nat. Mater.* **2019**, *18*, 1084.
[61] M. Mońka, I. Serdiuk, K. Kozakiewicz, E. Hoffman, J. Szumilas, A. Kubicki, S. Park, P. Bojarski, *J. Mater. Chem. C* **2022**, *10*, 7925.
[62] J. Kaminski, T. Böhmer, C. Marian, *J. Phys. Chem. C* **2024**, *128*, 13711.
[63] P. Dos Santos, D. de Sa Pereira, C. Oh, N. Kukhta, H. Lee, J. Lee, A. Monkman, *J. Phys. Chem. C* **2024**, *128*, 16308.
[64] F. Plasser, *J. Chem. Phys.* **2020**, *152*, 8.
[65] I. Serdiuk, M. Mońka, K. Kozakiewicz, B. Liberek, S. Bojarski, P. Park, *J. Phys. Chem. B* **2021**, *125*, 2696.
[66] F. Bloom, W. Wagemans, B. Koopmans, *Jpn. J. Appl. Phys.* **2008**, *103*, 7.
[67] E. Speckmeier, T. Fischer, K. Zeitler, *J. Am. Chem. Soc.* **2018**, *140*, 15353.
[68] N. Jamel, W. Lin, M. AbdWahab, D. Volyniuk, M. Gužauskas, A. Supangat, N. Nordin, F. Nasir, M. Ghasemi, K. Bareikaite, A. Monkman, T. Y. Seng, G. B. Hing, J. Vidas Grazulevicius, A. Ariffin, *ChemPhotoChem* **2024**, *8*, 202400138.
[69] N. S. Mohd J., L. Skhirtladze, A. Hussein, Y. Ma, K. Woon, M. Abdulwahab, J. Grazulevicius, A. Ariffin, *ACS Omega* **2024**, *9*, 50446.

[70] D. Weber, R. Heimburger, G. Schondelmaier, T. Junghans, A. Zetzl, D. R. T. Zahn, D. Schondelmaier, *SN Appl. Sci.* **2023**, *5*, 21.
[71] H. Yoshida, *J. Electron Spectrosc. Relat. Phenom.* **2015**, *204*, 116.
[72] P. Erdman, E. Zipf, *Rev. Sci. Instrum.* **1982**, *53*, 225.
[73] M. J. Frisch, G. W. Trucks, H. B. Schlegel, G. E. Scuseria, M. A. Robb, J. R. Cheeseman, G. Scalmani, V. Barone, G. A. Petersson, H. Nakatsuji, X. Li, M. Caricato, A. V. Marenich, J. Bloino, B. G. Janesko, R. Gomperts, B. Mennucci, H. P. Hratchian, J. V. Ortiz, A. F. Izmaylov, J. L. Sonnenberg, D. Williams-Young, F. Ding, F. Lipparini, F. Egidi, J. Goings, B. Peng, A. Petrone, T. Henderson, D. Ranasinghe, et al., *Gaussian 16 Revision C.02*, Gaussian Inc. Wallingford CT, **2016**.
[74] M. Streiter, T. Fischer, C. Wiebeler, S. Reichert, J. Langenickel, J. Reichert, S.and Langenickel, K. Zeitler, C. Deibel, *J. Phys. Chem. C* **2020**, *124*, 15007.
[75] B. de Souza, *Angew. Chem., Int. Ed.* **2025**, e202500393.
[76] Y. Ma, A. Hussein, *ChemistrySelect* **2022**, *7*, 202202354.
[77] Y. Ma, *KST48: A Powerful Tool for MECP locating, available from*, https://github.com/RimoAccelerator/KST48 (accessed: July 2025).
[78] F. Neese, *WIRES Comput. Molec. Sci.* **2012**, *2*, 73.
[79] F. Neese, *WIRES Comput. Molec. Sci.* **2022**, *12*, e1606.
[80] F. Plasser, *TheoDORE: A package for theoretical density, orbital relaxation, and exciton analysis, available from*, https://theodore-qc.sourceforge.io/ (accessed: July 2025).